



## Correlating inter-particle forces and particle shape to shear-induced aggregation/fragmentation and rheology for dilute anisotropic particle suspensions: A complementary study via capillary rheometry and *in-situ* small and ultra-small angle X-ray scattering

Anthony J. Krzysko<sup>a,b</sup>, Elias Nakouzi<sup>b</sup>, Xin Zhang<sup>b</sup>, Trent R. Graham<sup>b</sup>, Kevin M. Rosso<sup>b</sup>, Gregory K. Schenter<sup>b</sup>, Jan Ilavsky<sup>c</sup>, Ivan Kuzmenko<sup>c</sup>, Matthew G. Frith<sup>c</sup>, Cornelius F. Ivory<sup>d</sup>, Sue B. Clark<sup>a,b</sup>, Javen S. Weston<sup>e</sup>, Katie M. Weigandt<sup>f</sup>, James J. De Yoreo<sup>b,g</sup>, Jaehun Chun<sup>b,\*</sup>, Lawrence M. Anovitz<sup>h,\*</sup>

<sup>a</sup> Department of Chemistry, Washington State University, Pullman, WA 99164, United States

<sup>b</sup> Pacific Northwest National Laboratory, Richland, WA 99354, United States

<sup>c</sup> Argonne National Laboratory, 9700 S. Cass Ave., Bldg. 433A, Argonne, IL 60439, United States

<sup>d</sup> The Gene and Linda Vieland School of Chemical Engineering and Bioengineering, Washington State University, Pullman, WA 99164, United States

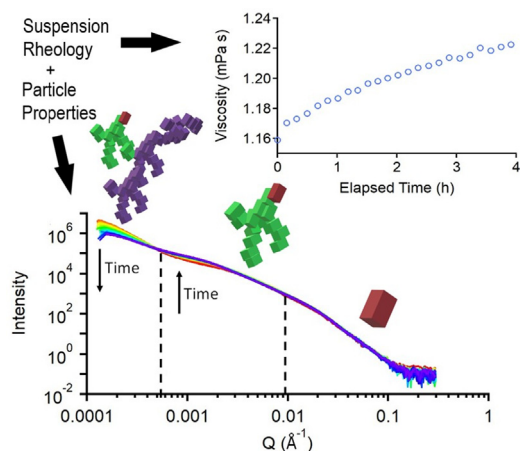
<sup>e</sup> Russell School of Chemical Engineering, University of Tulsa, Tulsa, OK 74104, United States

<sup>f</sup> Center for Neutron Research, stop 6102, National Institute of Standards and Technology, Gaithersburg, MD 20889-6102, United States

<sup>g</sup> Department of Materials Science and Engineering, University of Washington, Seattle, WA 98195, United States

<sup>h</sup> Chemical Sciences Division, MS 6110, Oak Ridge National Laboratory, Oak Ridge, TN 37831-6110, United States

### GRAPHICAL ABSTRACT



### ARTICLE INFO

#### Article history:

Received 10 March 2020

### ABSTRACT

**Hypothesis:** Understanding the stability and rheological behavior of suspensions composed of anisotropic particles is challenging due to the complex interplay of hydrodynamic and colloidal forces. We propose

\* Corresponding authors.

E-mail addresses: [anthony.krzysko@wsu.edu](mailto:anthony.krzysko@wsu.edu), [anthony.krzysko@pnnl.gov](mailto:anthony.krzysko@pnnl.gov) (A.J. Krzysko), [elias.nakouzi@pnnl.gov](mailto:elias.nakouzi@pnnl.gov) (E. Nakouzi), [xin.zhang@pnnl.gov](mailto:xin.zhang@pnnl.gov) (X. Zhang), [trenton.graham@pnnl.gov](mailto:trenton.graham@pnnl.gov) (T.R. Graham), [kevin.rosso@pnnl.gov](mailto:kevin.rosso@pnnl.gov) (K.M. Rosso), [greg.schenter@pnnl.gov](mailto:greg.schenter@pnnl.gov) (G.K. Schenter), [ilavsky@aps.anl.gov](mailto:ilavsky@aps.anl.gov) (J. Ilavsky), [kuzmenko@aps.anl.gov](mailto:kuzmenko@aps.anl.gov) (I. Kuzmenko), [mfrith@anl.gov](mailto:mfrith@anl.gov) (M.G. Frith), [cfivory@wsu.edu](mailto:cfivory@wsu.edu) (C.F. Ivory), [s\\_clark@wsu.edu](mailto:s_clark@wsu.edu), [sue.clark@pnnl.gov](mailto:sue.clark@pnnl.gov) (S.B. Clark), [jsw7755@utulsa.edu](mailto:jsw7755@utulsa.edu) (J.S. Weston), [kathleen.weigandt@nist.gov](mailto:kathleen.weigandt@nist.gov) (K.M. Weigandt), [james.DeYoreo@pnnl.gov](mailto:james.DeYoreo@pnnl.gov), [jjdy@uw.edu](mailto:jjdy@uw.edu) (J.J. De Yoreo), [jaehun.chun@pnnl.gov](mailto:jaehun.chun@pnnl.gov) (J. Chun), [anovitzlm@ornl.gov](mailto:anovitzlm@ornl.gov) (L.M. Anovitz).

<https://doi.org/10.1016/j.jcis.2020.04.016>

0021-9797/© 2020 Published by Elsevier Inc.

Revised 3 April 2020  
 Accepted 3 April 2020  
 Available online 25 April 2020

**Keywords:**

Boehmite  
 Aggregation  
 Fragmentation  
 Rheology  
 Small-angle X-ray scattering  
 Ultra-small-angle X-ray scattering  
 Wide-angle X-ray scattering  
 Power-law fluid

that orientationally-dependent interactions resulting from the anisotropic nature of non-spherical subunits strongly influences shear-induced particle aggregation/fragmentation and suspension rheological behavior.

**Experiments:** Wide-, small-, and ultra-small-angle X-ray scattering experiments were used to simultaneously monitor changes in size and fractal dimensions of boehmite aggregates from 6 to 10,000 Å as the sample was recirculated through an *in-situ* capillary rheometer. The latter also provided simultaneous suspension viscosity data. Computational fluid dynamics modeling of the apparatus provided a more rigorous analysis of the fluid flow.

**Findings:** Shear-induced aggregation/fragmentation was correlated with a complicated balance between hydrodynamic and colloidal forces. Multi-scale fractal aggregates formed in solution but the largest could be fragmented by shear. Orientationally-dependent interactions lead to a relatively large experimental suspension viscosity when the hydrodynamic force was small compared to colloidal forces. This manifests even at low boehmite mass fractions.

© 2020 Published by Elsevier Inc.

## 1. Introduction

Predicting the stability and aggregation behavior of nanoparticles, especially under flow, is important to several fields in engineering, materials science, and chemistry including water treatment [1], polymer latex manufacturing [2], paper manufacturing [3], protein stability/folding [4], and transport of monoclonal antibodies [5]. However, shear-induced aggregation and fragmentation of colloidal dispersions is complex and heavily influenced by the physical parameters [6,7] and surface/solution chemistry of the system [8–10] through their coupling to flow characteristics. These are directly correlated to particle interactions that are often understood through a delicate balance between van der Waals ( $V_{vdW}$ ) and electrostatic ( $V_{ele}$ ) interactions in the context of the Derjaguin-Landau-Verwey-Overbeek (DLVO) theory. More complex interactions such as hydration and steric repulsive forces have been addressed using adjustments to DLVO theory, but are often system specific [11–14]. For example, ion-specific adsorption can lead to variations in particle surface charges manifesting as ion-specific effects [15]. Additional complications arise in concentrated ionic systems, where significant deviations from Debye screening lengths are expected in the dilute limit, leading to long-range electrostatic forces, and have been reported in concentrated aqueous salt solutions and ionic liquids [16,17]. These affect the stability of colloidal particles, creating challenges in predicting and controlling particle aggregation [18], which have been addressed using kinetic approaches (typically 2nd order kinetics [19]). Such aggregation kinetics can be characterized by a rate coefficient ( $k_{agg}$ ) that depends on particle interactions as well as external “driving” forces such as Brownian, shear, and differential gravitational forces. The importance of particle interactions to aggregation kinetics has been represented as a stability ratio ( $W$ ), given as the ratio of the rate coefficients ( $W = k_0 k_{agg}^{-1}$ ) [20], where  $k_0$  denotes an “ideal” rate coefficient without inter-particle forces.

Aggregation under flow has been studied extensively [20]. The interplay of shear and colloidal forces has been fairly well established [21], and the basic rheological properties of colloidal dispersions at a wide range of volume fractions have been described on the basis of inter-particle forces [22], especially using a hard sphere assumption [23]. However, connecting aggregate properties, such as size and shape (i.e. fractal dimensions ( $d_f$ )), to rheological properties remains an active field of research, being studied using a variety of scattering techniques [24–28]. For example, thixotropy, and other non-reversible processes are still not well understood, especially for complex (e.g. inhomogeneous) aggregates [29]. For systems with broad, inhomogeneous size distributions, small angle X-ray scattering (SAXS) and small angle neutron scattering (SANS) have been especially useful for correlating

rheological properties to aggregate properties [30–32]. Particle shape can greatly affect the stability of aggregates (and thus rheology), but is difficult to quantify and predict [33], and fragmentation and aggregate restructuring under flow are also poorly understood because of the complexity of the process [34]. While models have been developed for predicting fragmentation events by estimating hydrodynamic, van der Waals, and repulsive interactions using Stokesian dynamics for monodisperse systems [35,36], quantifying and predicting the rheological responses for non-spherical polydisperse materials is challenging.

The physical and chemical complexities described above exist in virtually all practical applications of slurry flow. One important example is treatment of the wastes stored in tanks at the Hanford Site in Washington state, United States [37]. The rheology of these materials involves a number of complicating factors, including high levels of radioactivity, elevated pH (>12), high ionic strength, and non-spherical particle shapes, which combine to influence the aggregation and rheological behavior of the slurries and sludges in the waste tanks. The mineralogy of these materials also adds to the complexity. While many solid phases are present, the most common are aluminum (oxy)hydroxides. Of these, boehmite ( $\gamma$ -AlO(OH)) is of particular concern as it forms complex aggregates that affect solutions rheology, complicating waste recovery and treatment [38,39]. Furthermore, like many other minerals, boehmite nanoparticles have a platelet-like particle geometry composed of sharp-edges and significant three-dimensional anisotropy (see TEM image in Fig. S1). It is not well understood how non-spherical geometry, coupled with the complex solution structure around boehmite nanoparticles, affects macroscopic properties such as aggregation, precipitation, and response to flow, especially in the aforementioned complex environments [40,41].

A number of explorations into how particle forces influence aggregation and the resultant boehmite nanoparticle morphology at elevated ionic strengths and pH have been performed [42,43]. Using small- and ultra-small-angle neutron and X-ray scattering, the discrete size distributions and fractal dimensions ( $d_f$ ) of the aggregates were found to be highly dependent on solution conditions. For instance, approximately 100 times less  $\text{Ca}(\text{NO}_3)_2$  than  $\text{NaNO}_3$  was needed to produce similar changes to aggregate structures [42]. Analysis of Brownian aggregation of boehmite nanoparticles using dynamic light scattering [43] demonstrated that particle shape anisotropy strongly influenced boehmite particle aggregation. Significant deviations were observed between calculated stability ratios based on spherical particles ( $W_{sph}$ ) and those observed experimentally ( $W_{exp}$ ). Interestingly, a very large ( $\approx 10^4$ ) stability ratio was reported at pH = 9 without additional salt, close to point of zero charge (PZC) of boehmite [44,45]. Under these conditions attractive van der Waals forces should dominate

repulsive electrostatic forces, leading to a low stability ratio. The large stability was attributed to orientation-dependent colloidal and hydrodynamic interactions that do not exist for spherical particles. Despite these studies, however, how changes in boehmite nanoparticle aggregation emerge from the unique physicochemical nature of boehmite forces, and their impact on rheology, have not been clearly understood.

In this study, the effects of flow on the aggregation and fragmentation of boehmite nanoparticles were investigated as a function of cumulative shear stress, as was the question of whether the effects of shape anisotropy on aggregation structures and kinetics manifests under shear in a manner that contrasts with the behavior of typical spherical particles. An experimental method was developed that allows monitoring the time evolution of boehmite aggregation and fragmentation resulting from the interplay of flow and particle interactions using *in-situ* measurements of hierarchal aggregate structures and slurry rheology. This combined capillary rheometry with *in-situ* small-angle X-ray scattering (SAXS), ultra-small-angle X-ray scattering (USAXS), and wide-angle X-ray scattering (WAXS) to quantify boehmite particle behavior at scales from 6 to 10,000 Å with a time delay of a few minutes per analysis over several hours. Additionally, computational fluid dynamics (CFD) was used to more rigorously describe the flow and calculate the shear dissipation energy to explain aggregate property changes in terms of the total and rate of energy input.

## 2. Experimental

### 2.1. Boehmite synthesis

Boehmite nanoparticles were prepared using a method detailed elsewhere [46] and briefly summarized here. Aluminum nitrate nonahydrate (250 mmol,  $\text{Al}(\text{NO}_3)_3 \cdot 9\text{H}_2\text{O}$ , purity  $\geq 98\%$ , Sigma-Aldrich) was dissolved in 1000 mL of deionized water followed by sufficient additions of  $3 \text{ mol dm}^{-3}$  sodium hydroxide (NaOH, purity  $\geq 98\%$ , Sigma-Aldrich) to achieve a final pH of 10. The mixture was stirred for 1 h at room temperature and the resulting gel-like precipitates were collected by centrifugation and washed ( $\text{DI-H}_2\text{O}$ ,  $\times 3$ ) to remove residual ions. The washed gel was dispersed into  $0.1 \text{ mol dm}^{-3}$  NaOH solution (pH = 13) with a ratio of 0.4 g gel : 1 g NaOH solution and sealed into a 125 mL PTFE-lined stainless steel pressure vessel (Model 4748, Parr Instrument

Company). This was placed in a rotary oven at  $120^\circ\text{C}$  and 10 rpm for 2 days, after which the sample was allowed to cool, collected via centrifugation, washed ( $\text{DI-H}_2\text{O}$ ,  $\times 3$ ), and dried at  $50^\circ\text{C}$ . The product was characterized using transmission electron microscopy (TEM) and powder X-ray diffraction (pXRD) [46]. A representative TEM image and pXRD plot are shown in Figs. S1 and S2, respectively.

### 2.2. Boehmite slurry preparation

To prepare a slurry for capillary rheometry the as-synthesized boehmite nanoparticles were dispersed in an unbuffered pH 9 solution (NaOH,  $\geq 98\%$ , Sigma-Aldrich) so that the suspension was composed of 2.5 wt% boehmite (g boehmite/g aqueous solution). The slurry was dispersed by briefly sonicating the mixture (Fisher Scientific model D100, 22.7 kHz) at a power setting of 13 W (3 pulses of  $\sim 20$  s each), then loaded into a 10 mL syringe for injection into the capillary rheometer and subsequent USAXS/SAXS/WAXS measurements.

### 2.3. Flow system and capillary rheometer

The boehmite slurries (0.025 g boehmite/g NaOH solution) described above were cycled through a capillary rheometer (Fig. S3). The differences expected in Couette flow and Poiseuille flow of aluminum (oxy)hydroxide systems have been discussed in detail in our previous work [47]. A schematic of the system is shown in Fig. 1. Two opposing syringes (C and D) were mounted onto a motor-driven syringe pump (A). Initially, syringe C held the boehmite slurry and syringe D was empty. After setting the flow rate, the drive rod (B) pushed the plunger of syringe C, while simultaneously pulling that of syringe D. The slurry was transported through 1 m of PEEK tubing (E), the quartz tube (F), then a second 1 m of PEEK tubing (G) to the second syringe (D). Then the procedure was repeated in opposite direction. The quartz tube was used: (1) because it had the appropriate internal diameter to accommodate the X-ray beam and (2) to prevent degradation due to beam damage. Two pressure transducers (H and I) measured the pressure drop during flow. Each half-cycle was paused approximately halfway to perform USAXS, SAXS, and WAXS measurements. By stopping the cycle at the halfway point, the likelihood of measurements being made on material that had not fully cycled through the two lengths of capillary tube was reduced. Prior

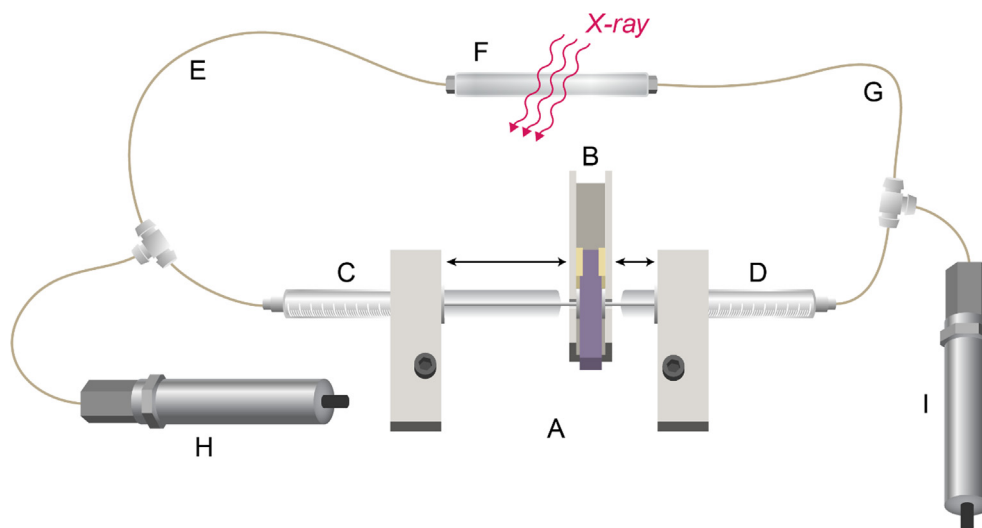


**Fig. 1.** Schematic of the capillary rheometer flow system. An aluminum stand (A) holds a motor driven syringe attachment (B) on which two syringes are mounted (C and D). Two pieces of PEEK tubing (E and G) are the major sources of shear force and the quartz tube (F) is where the X-ray measurements are performed.

to the first cycle, a pre-shearing half-cycle (slurry moved from syringe C to syringe D) was performed at the same flow rate as the run. No X-ray measurements were made during this pre-cycle. The slurry was cycled in the rheometer until no further changes were observed in the (U)SAXS measurements.

For rheological calculations the capillary rheometer was simplified to only consider the two longer PEEK tubes (E and G in Fig. 1) and the quartz tube (F in Fig. 1). All other contributions to the shear stress ( $\tau$ ) could be ignored. The quartz tube had a length ( $l_c$ ) of 9 cm and an ID ( $d_c$ ) of 4 mm. Each piece of PEEK tubing (E and G in Fig. 1) had constant length ( $l_t$ ) of 1 m, and two ID values ( $d_t$ ) were used: 0.1106 and 0.0508 cm. The volumetric flow rate ( $Q_f$ ) was varied from experiment to experiment. Six runs were performed using freshly prepared slurries. The parameters used to characterize the different flow conditions and run labels are presented in Table 1.

Each of the six experiments in Table 1 can be uniquely identified by its characteristic shear rate ( $\dot{\gamma}$ ). In order to calculate the shear rate, the viscosity must first be calculated. Assuming an incompressible laminar flow, the Hagen-Poiseuille equation for a circular tube geometry (Eq. (1)) can be used to calculate the viscosity ( $\eta_{sus}$ ) of the boehmite suspension as:

$$\eta_{sus} = \frac{\pi \Delta P R^4}{8 Q_f L} \quad (1)$$

where  $\Delta P$  is the measured pressure drop in the tube,  $R$  is the internal radius of the tube,  $Q_f$  is the flow rate, and  $L$  is the tube length. It can be shown (S. Eqs. (1) and (2)) that the average shear rate ( $\dot{\gamma}_{avg}$ ) can be calculated as:

$$\dot{\gamma}_{avg} = - \frac{\Delta P R}{3 \eta_{sus} L} \quad (2)$$

Because the diameter varies between the capillary tubing and the quartz tube (E, F, and G in Fig. 1), the issue becomes choosing appropriate values for  $R$  and  $L$ . If the flow remains laminar as the slurry is transported from the PEEK tubing into and out of the quartz tube, the quartz tube can largely be ignored because the ratio of the inner diameters of the tubes,  $d_c/d_t \approx 8$  for the narrowest PEEK tubing, and the length of the quartz tube is significantly less than that of the PEEK tubing ( $L_c/2L_t \approx 22.2$ ). Therefore, as a first approximation,  $R = r_t$  and  $L = 2l_t = 2$  m. The validity of ignoring the quartz tube to simplify the rheological calculations, and the error associated with expansion and contraction of the suspension into and out of the quartz tube were further explored using computational fluid dynamics (CFD, see below).

The Reynolds number ( $Re$ ) was calculated for each run (Eq. (3)) as:

$$Re = \frac{Q_f d_t}{\nu A} \quad (3)$$

where  $\nu$  is the kinematic viscosity of the suspension, which can be assumed to be close to that of water because of the small amount of boehmite (2.5 wt%) in the slurry, and  $A$  is the cross-sectional area of

the tube. The relative influences of advection and diffusion on particle motion can be evaluated using the Peclet number ( $Pe$ ):

$$Pe = \frac{6\pi\mu a^3 \dot{\gamma}_{avg}}{kT} \quad (4)$$

where  $a$  is the characteristic size of the particle (e.g., its hydrodynamic radius),  $\mu$  is the solvent viscosity without the suspended solid (note that  $Pe$  refers to the forces on a particle suspended in the liquid),  $k$  is the Boltzmann constant,  $\dot{\gamma}_{avg}$  is the average shear rate, and  $T$  is the temperature. The larger the Peclet number, the more important is advection (i.e. hydrodynamic force on the particle) relative to diffusion.

#### 2.4. USAXS, SAXS, WAXS

Scattering experiments were performed at the Advanced Photon Source (Argonne National Laboratory, Lemont, Illinois) on beamline 9-ID-C [48]. The X-ray incident wavelength ( $\lambda$ ) was 0.5904 Å (21 keV). The beam size was  $\approx 0.8$  (width)  $\times$  0.2 (height) mm<sup>2</sup> for SAXS and WAXS and 0.8 (width)  $\times$  0.8 (height) mm<sup>2</sup> for USAXS. Each USAXS measurement was acquired for 60 s with a scattering vector,  $Q$  (whose modulus  $q = (4\pi \sin \theta)\lambda^{-1}$ ) [49] ranged from 0.0001 to 0.6 Å<sup>-1</sup> with a resolution  $\approx 0.00008$  Å<sup>-1</sup>. The SAXS and WAXS data were acquired for 30 s each over  $Q$  ranges of 0.03–1.3 and 1–7 Å<sup>-1</sup>, respectively. Data were reduced using the INDRA and NIKA [50] software packages and analyzed using the IRENA software package [51].

The reduced USAXS data were fitted using the unified fit model [52]. This assumes the total scattering of the system  $I(Q)$  is composed of  $N$  individual scattering levels with index  $i$ :

$$I(Q) = \sum_i^N I_i(Q) \quad (5)$$

Scattering from each level ( $I_i(Q)$ ) is given as:

$$I_i(Q) \approx G_i e^{-\frac{Q^2 R_{g,i}^2}{3}} + e^{-\frac{Q^2 R_{gco}^2}{3}} B_i \left[ \frac{\left( \text{erf} \left( \frac{Q R_{g,i}}{6z} \right) \right)^3}{Q} \right]^{P_i} \quad (6)$$

where  $I_i$  is the intensity of the level,  $Q$  is the scattering vector that describes the difference between the incident and scattered waves,  $R_{g,i}$  is the radius of gyration of the  $i^{\text{th}}$  level,  $R_{gco}$  is the radius of gyration cutoff (terminates at  $R_{g,n-1}$ ),  $G_i$  is the Guinier prefactor,  $B_i$  is the power-law prefactor, and  $P_i$  is the power-law slope (and the negative of the mass fractal dimension,  $d_f$ ) corresponding to the  $i^{\text{th}}$  level. The unified fit model was chosen for the analysis due to its flexibility to parameterize the scattering intensity over a large range in  $Q$ , while fitting multiple populations. While the unified fit model is a simplistic analysis that can sometimes have too much flexibility [53,54], it allows the system to be described using easily understood parameters (e.g.,  $R_g$  and  $P$ ) that can provide important insights into the changes occurring in the system without imposing

**Table 1**  
Run labels and characteristic flow parameters using the Newtonian model.

Run Label	$d_t$ (cm)	$Q_f$ (cm <sup>3</sup> min <sup>-1</sup> )	$\Delta P$ (kPa)	$\eta_{sus,i}$ (mPa s)	$\dot{\gamma}_{avg}^c$ (s <sup>-1</sup> )	$Re$	$Pe$ (200nm)
<b>A</b>	0.1106	0.684	4.5 ± 0.7	3.3 ± 0.5 <sup>a</sup>	60	13	1.9
<b>B</b>	0.1106	3.43	8.0 ± 0.4	1.9 ± 0.1 <sup>a</sup>	290	66	9.3
<b>C</b>	0.0508	0.684	15.5 ± 0.5	1.24 ± 0.04 <sup>b</sup>	600	29	19
<b>D</b>	0.1106	17.1	24.3 ± 0.4	1.43 ± 0.04 <sup>b</sup>	1400	330	47
<b>E</b>	0.0508	3.43	80.7 ± 1.2	1.21 ± 0.04 <sup>b</sup>	3000	140	96
<b>F</b>	0.0508	17.1	402 ± 6	1.16 ± 0.03 <sup>b</sup>	15,000	710	480

<sup>a</sup> Error is  $\pm 1$  standard deviation.

<sup>b</sup> Error  $\approx 3\%$  based upon propagated uncertainty (one standard error).

unsupported assumptions such as monodispersity or a pre-defined structure factor. Furthermore, it will be shown that the changes in the parameters obtained by the unified fit model reflect qualitative changes in the USAXS data.

### 3. Results

#### 3.1. Slurry viscosity and rheology

The values of the initial suspension viscosity ( $\eta_{sus,i}$ ),  $\dot{\gamma}_{avg}$ ,  $Re$ , and  $Pe$  measured after the pre-shearing cycle calculated using Eqs. (1), (2), (3), and (4), respectively, are shown in Table 1.  $Re$  values indicate the flow was laminar, assuming the contribution from the quartz tube was negligible. In order to calculate  $Pe$ , which assumes that the particles are spheres, a value of 200 nm was chosen as the representative hydrodynamic particle radius ( $a$ ). This was calculated from the average size of the level 2 aggregates (calculated using the model described below) averaged as a sphere, as the expected time scales of their rotational and translational motions are short relative to that of the measurement (see SI for details).

The change in  $\Delta P$  as a function of time for each of the experiments is shown in Fig. S4. The  $\Delta P$  for runs **A** and **B** was essentially constant during the experiment. Therefore,  $\eta_{sus} = \eta_{sus,i}$  and was taken as the average of 14 and 28 values measured during runs **A** and **B**, respectively (Fig. S4). As the shear rate was increased, the suspension viscosity decreased, with  $\eta_{sus} = 3.3 \pm 0.5$  mPa s at  $\dot{\gamma}_{avg} = 60$  s<sup>-1</sup> (run **A**) and  $\eta_{sus} = 1.16 \pm 0.06$  mPa s at  $\dot{\gamma}_{avg} = 15000$  s<sup>-1</sup> (run **F**). Unlike runs **A** and **B**, for runs **C** – **F**  $\Delta P$  increased during the run and, therefore, so did  $\eta_{sus}$  (Fig. 2). Of the six experimental runs, the change in  $\eta_{sus}$  with cycling was greatest for run **E** (1.2 mPa s).

#### 3.2. Mathematical modeling and simulation

When the Hagen-Poiseuille equation was used to extract viscosities from the data, it was found that the experimental viscosities decrease by about a factor of 2 as the Reynolds number increases from ~10 to ~1000 (Table 1). This is a large enough variation that it will have an appreciable impact on the calculation of the pressure drop, shear rate, and power dissipation in the capillary, as well as the extent of mixing in the quartz cell. Since the Hagen-Poiseuille expression is derived from the Navier-Stokes

equation applying Newton's Law for the constitutive equation for the viscous stress, Newton's Law was compared with a power-law relationship that could account for the observed shear-thinning. The simplest expression is the Ostwald-de Waele power-law which, for unidirectional flow in a capillary, can be represented as:

$$\mu_c = m|\dot{\gamma}|^{n-1} \quad (7)$$

where  $\mu_c$  is the power-law viscosity,  $n$  is a power law exponent and  $m$  is an empirical parameter, both of which are fitted to experimental data. Given Eq. (7), for flow in capillaries with different diameters the Hagen-Poiseuille equation becomes:

$$\frac{Q_f}{d_t^3} = \frac{\pi}{8} \frac{n}{3n+1} \frac{1}{m^{1/n}} \left( \frac{\Delta P}{4L} d_t \right)^3 \quad (8)$$

where  $Q_f$ ,  $L$ , and  $\Delta P$  are as defined as for Eq. (1),  $m$  and  $n$  are the constants just defined by Eq. (7), and  $d_t$  is the inner diameter of the PEEK tubing. Fitting the volumetric flow against the pressure drop (Table 1) [55,56] yields  $m = 1.91 \times 10^{-3} \pm 17.5\%$  [Pa s<sup>n</sup>] and  $n = 0.949 \pm 1.9\%$  (Fig. S5). The fact that  $n$  is close to one suggests the suspension viscosities obtained from the Hagen-Poiseuille equation are reasonable.

In order to better understand the physics of the capillary rheometer, a flow simulation was performed using the laminar flow physics model in the CFD module in COMSOL Multiphysics® v5.4 (COMSOL AB, Sweden). The model geometry, which had to be rendered in full 3D due to an asymmetry that emerged at moderate  $Re$ , was composed of two 1-meter long capillaries joined by the optical window. All three parts of the model were represented as straight, right cylinders with fixed diameters (Table 1). This model assumes an incompressible laminar flow and the Ostwald-de Waele power-law model [57], (Eq. (7)), no-slip boundary conditions, a fully-developed/symmetric inlet flow, and atmospheric pressure at the outlet.

In the simulation, the following governing equations were solved numerically:

$$\nabla \cdot \mathbf{v} = 0 \quad (9a)$$

$$\rho \frac{\partial \mathbf{v}}{\partial t} + \rho \mathbf{v} \cdot \nabla \mathbf{v} = -\nabla p + \nabla \cdot \mu_c [\nabla \mathbf{v} + (\nabla \mathbf{v})^T] \quad (9b)$$

where  $\mathbf{v}$  is the velocity,  $\rho$  is the suspension density, and  $p$  is the pressure. The power law model Reynolds number ( $Re_c$ ) and power law viscosity averaged over the cross-section of the tube geometry ( $\langle \mu_c \rangle$ ) were calculated using S.Eq 3 and S.Eq 4, respectively (details in the SI, Table S1). The energy dissipated per pass (i.e. energy rate) through the rheometer was calculated using the power-law model. This allowed changes in the aggregate size and shape parameters to be compared to the cumulative amount of energy expended as well as the rate of energy release, providing a method to estimate fragmentation and aggregation of suspended boehmite particles exposed to other forms of mechanical energy (e.g. pumping, sonication [42]) during tank waste treatment. The power dissipation rate was calculated in COMSOL Multiphysics® (S.Eq (5)).

Table 2 shows the calculated excess pressure drop due to expansion/contraction associated with the change in internal diameter between the capillaries and the optical window. While oscillations after expansion into the quartz tube were observed (Fig. S6), the contributions of the expansion/contraction on the pressure drop to the overall drag were shown to be always positive and less than ~2.2% of the total  $\Delta P$ , even at the highest  $Re_c$  investigated. This indicates that the effects of transitions to and from the optical window are negligible. It should be noted, however, that the excess pressure drop increases more rapidly at higher  $Re_c$  than at low  $Re_c$ , although the calculated power-law viscosity does not.

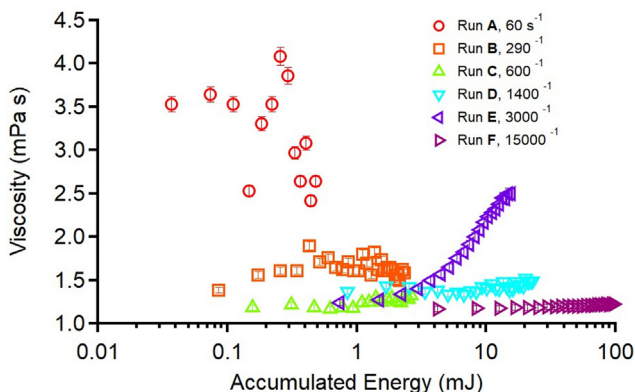


**Fig. 2.** Calculated  $\eta_{sus}$  values as the slurry was cycled through the capillary rheometer for runs **A**–**F**. The errors were taken to be 2.5% of the calculated value, determined from the precision of the pressure transducer (within the size of the markers). Each point represents an individual half cycle of the rheometer (a transfer of the fluid from one syringe to the other, but not back). The accumulated energy is proportional to the number of half-cycles performed on the slurry (see following section). The energy dissipation per half-cycle is shown in Table 2.

**Table 2**  
The flow and structure parameters calculated using the mathematical modeling and simulations. The results of fitting the parameters corresponding to the size and shape of the initial boehmite aggregates (Eq. (8)) after pre-shearing are also shown.

Run Label	Excess $\Delta P$ (Pa)	Energy Per Half-Cycle (mj)	$R_{g,1}^0$ (Å)	$R_{g,2}^0$ (Å)	$-P_2^0$	$-P_3^0$
A	6.6	0.018	$82 \pm 4$	$2510 \pm 250$	$2.07 \pm 0.01$	$1.6 \pm 0.4$
B	16.0	0.086	$107 \pm 10$	$2000 \pm 200$	$1.70 \pm 0.02$	$1.8 \pm 0.4$
C	44.9	0.078	$86 \pm 10$	$1990 \pm 430$	$2.04 \pm 0.03$	$2.2 \pm 0.1$
D	245.2	0.422	$85 \pm 8$	$1600 \pm 170$	$2.16 \pm 0.03$	$2.4 \pm 0.1$
E	285.6	0.371	$102 \pm 7$	$2158 \pm 250$	$2.15 \pm 0.02$	$3.0 \pm 0.1$
F	8631.0	2.10	$76 \pm 8$	$1320 \pm 80$	$2.21 \pm 0.02$	$3.3 \pm 0.2$

### 3.3. USAXS, SAXS, and WAXS

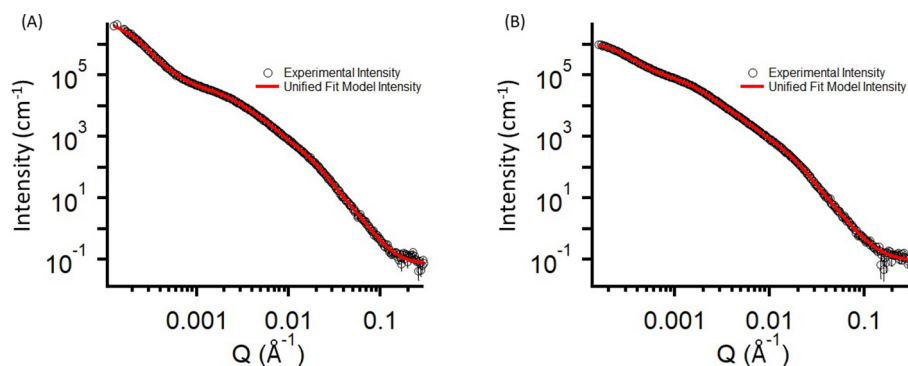
The broad  $Q$  range of the scattering data (approximately five decades), and the rapid data acquisition provided by the 9-ID-C spectrometer, allowed aggregation dynamics to be monitored in real time across multiple length scales. It should be noted that shear-induced rotation/alignment of the aggregates may occur during slurry cycling. However, this was not observed. There are two possible reasons for this result. First, as described above, the measurements were done in the center of the quartz glass tube. Turbulent expansion occurs at the inlet of this tube as its ID is significantly larger than the PEEK tubing (Fig. S6). While the energetic contribution of this expansion is small compared to the shear force in the narrow tubing, any directional isotropy may be lost to “mixing” in the expansion process. Second, USAXS measurements were made with the flow paused, which may have allowed particle relaxation and the loss of any alignment present during flow. In the end, however, no anisotropy was observed.

Fig. S7 shows representative plots of the SAXS and WAXS data for run F. Interestingly, the intensities in both regions remained mostly unchanged over the course of the experiment. The broad peaks in the WAXS region (Fig. S7(B)) were present in each sample set and could indicate the presence of an amorphous phase [58]. These persisted throughout the experiment with no evidence of new phase formation. The well-defined peak at  $\approx 1 \text{ \AA}^{-1}$  (Fig. S7 (A)) is the first diffraction peak of the boehmite lattice. The remaining weak diffraction peaks of the boehmite lattice are shown in Fig. S7(B). Fig. 3 shows the initial and final experimental and fitted USAXS data for run F. Unlike the data in the SAXS and WAXS regions, clear changes are observed at these length scales at low and mid  $Q$ . The higher  $Q$  region of the USAXS data, however, remains unchanged (Fig. S8).

The unified fit model [51,52,59] was used to quantitatively evaluate changes in the USAXS region. This treats the data as a series of structural levels, each composed of a Guinier region at lower  $Q$ , and a power-law tail at higher  $Q$ . Each level describes a part of the

structure over a finite size range. The variables involved are described above. In these experiments the levels represent primary particles (level 1), aggregates of primary particles (level 2), and agglomerates of aggregates (level 3). However, the system is not expected to be monodisperse with respect to size or shape at any level. TEM imagery (Fig. S1) and reports in the literature both show that the particles and aggregates are polydisperse in both size and shape [42,43]. Furthermore, qualitative analysis of the USAXS data shows that levels 1 and 2 can be treated as uncorrelated, as significant variations in level 2 are not reflected in level 1. This makes physical sense, as the shearing force scales with particle size and thus is less impactful at high  $Q$ . However, levels 2 and 3 are correlated. Any “breakage” of the agglomerates (level 3) will likely result in a change at level 2 because this forms new level 2-sized particles. Moreover, if restructuring and aggregation occur in level 2, level 3 scattering may be affected. As there is no structural model that can describe such a complex system, a simplified approach – the unified fit model – was chosen to parametrize the different scattering regions observed in the USAXS data and show how they change over time (proportional to the number of cycles the slurry experienced). This allows a complex, polydisperse system to be understood using simple parameters that can provide insights into changes in the system and how they relate to changes in rheology. Most importantly, the parameters obtained using the unified fit model reflect the qualitative changes observed in the USAXS data (Fig. S8). The balance of particle forces can then be analyzed by comparing the parameters of the unified fit model to the rheological responses. Therefore, the particle interactions are implicitly, but not explicitly accounted for in the unified fit model at different flow conditions.

Three unified fit levels (Eq. (6)) were used to fit the USAXS data (Fig. S8). In most cases, fewer than 3 levels were inadequate. The same model was used in every case to enable comparisons. Because the model assumes the levels are a collection of hierarchical aggregates (primary particles, aggregates, and agglomerates) that can be modeled as mass fractals [27], the level 2 aggregates



**Fig. 3.** An example of the experimental USAXS intensity (black circles) and model intensity (red line) of the initial scan (A) and final scan (B) taken from run F. The data was fit using the unified fit model with 3 different levels as described. The fitting for the individual levels is shown in Fig. S9. The USAXS time evolution for each run can be seen in Fig. S8. (For interpretation of the references to colour in this figure legend, the reader is referred to the web version of this article.)

are composed of level 1 particles, and level 2 aggregates are the building blocks for level 3 agglomerates of aggregates. Thus,  $R_{g,i}$  and  $-P_i$  are the radius of gyration and mass fractal dimension of the  $i^{\text{th}}$  level aggregate [59].

An example fit and the individual levels that comprise it, is shown in Fig. S9. It is clear from this example that the model fits the data quite well. However, the lowest  $Q$  level (level 3) is not completely captured by the USAXS data, implying that aggregates form at scales larger than those measured. Thus, the value of the radius of gyration for this level,  $R_{g,3}$  is beyond the range of the instrument and could be not be fitted. Despite this limitation, the power law slope ( $P_3$ ) for this structural level was captured, requiring a third level in the model. To address this problem the value of  $R_{g,3}$  was fixed at  $10^{10}$  Å for all samples.

Fitted parameters for the initial state of each experiment after the pre-shearing half-cycle are shown in Table 2. The first level corresponds to “primary” particles whose radius (from the average  $R_{g,i}^0$  in Table 2) was  $90 \pm 12$  Å, in good agreement with the particle size determined by TEM (Fig. S1) and reported results using similar synthesis conditions [42,43,46]. The uncertainties were estimated by quantifying the relative impact of the fitted parameters on the overall fit. To do so each parameter was varied with the others kept constant through a finite range and the impact on the quality of the fit ascertained [51,60]. This method was used for selected USAXS scans for each sample. Note that the uncertainties originate from the anisotropic and polydisperse nature of the particles/aggregates indicated by TEM images (Fig. S1). The large uncertainty in  $R_{g,2}$  directly reflects the large distribution of sizes of the level 2 aggregates and the overlap in size between these and the level 3 agglomerates. This overlap restricts the region of  $Q$  used to fit  $R_{g,2}$  and  $P_3$  to a relatively small zone. Therefore, the statistical variation of  $R_{g,2}$  and  $P_3$  is relatively large. The uncertainty in  $P_2$  is low, however, due to the larger  $Q$  range used to determine its value. Despite the relatively large uncertainty in the  $R_{g,2}$  values, a clear decreasing trend was observed with increasing  $Pe$ . The initial value of the second level  $R_{g,2}$  (after a pre-shearing cycle) has been fit against the energy dissipated per half cycle (Fig. S10) to demonstrate that a trend with the influence of flow exists.

The changes to  $R_{g,2}$ ,  $-P_2$ , and  $-P_3$  as a function of accumulated energy are presented in Figs. 4–6, respectively, for each experiment. The accumulated energy was the energy per half cycle (Table 2) multiplied by the number of half cycles. This is also proportional to the elapsed time over which the slurries were cycled. The times per half-cycle are given in Table S1. As expected from

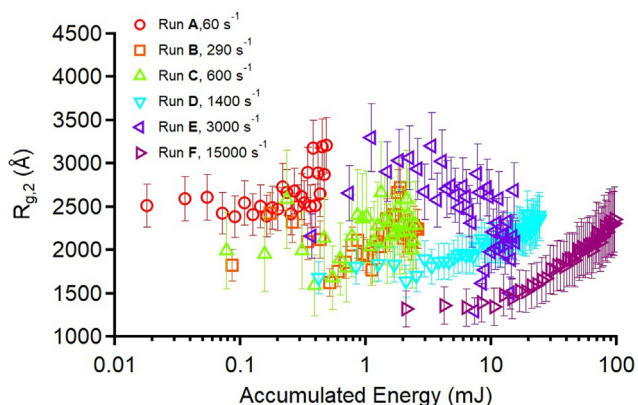


**Fig. 4.** The sizes of the level 2 boehmite aggregates obtained from the USAXS results monitored over the duration of the shear flow. The labels, **A** to **F**, correspond to the runs in Table 1. The accumulated energy corresponds to the number of cycles. The uncertainty was 10, 10, 22, 11, 12, and 6%, respectively for runs **A–F**.

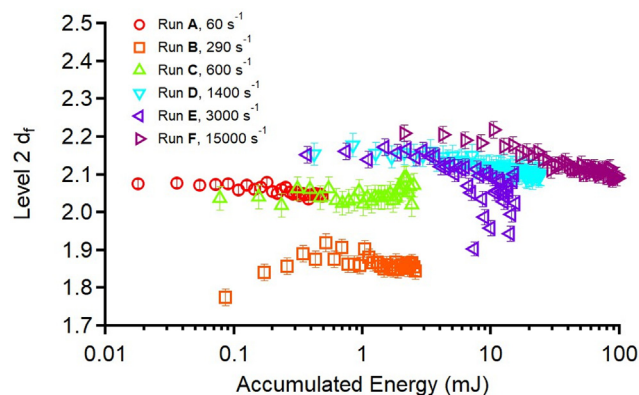


**Fig. 5.** The fractal dimensions of the level 2 aggregates ( $-P_2$ ) obtained from the USAXS results monitored during the experiment. Larger shear rates (i.e. stronger hydrodynamic forces) generally produce larger level 2  $d_f$  values. The labels, **A** to **F**, correspond to the runs listed in Table 1. The uncertainties were 0.5, 1.2, 1.5, 1.4, 0.9, and 6.1%, respectively for runs **A–F**.

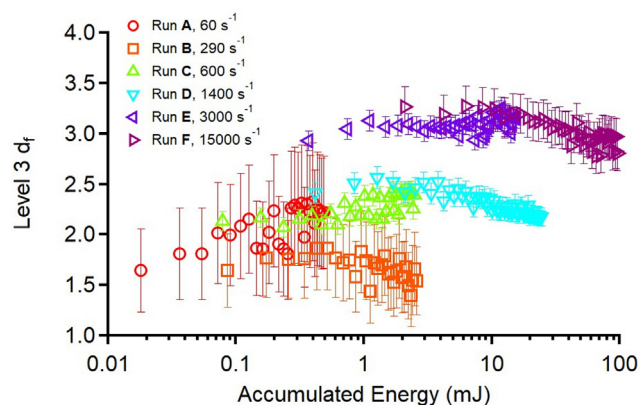


**Fig. 6.** The fractal dimensions of the level 3 aggregates ( $-P_3$ ) obtained from the USAXS results during the slurry cycling. The labels, **A** to **F**, correspond to the runs listed in Table 1. Note that the fractal dimensions for runs **E** and **F** are slightly larger than 3. This is likely due to fitting uncertainties. The uncertainties were 25, 22, 4.5, 4.2, 3.3, and 6.1%, respectively for runs **A–F**.

Fig. S8, the values for the smallest-size level (highest  $Q$ ) were not affected by the change in flow characteristics, indicating that no significant change occurred in the primary particles over the course of the experiment. Note that  $-P_1$  was held constant at 4 at this level to satisfy the sharp interface condition of Porod's law [52–54]. This power-law slope extends into the SAXS region until the first boehmite lattice diffraction peak appears at  $1 \text{ \AA}^{-1}$ . Generally,  $R_{g,2}$  decreases and  $-P_2$  and  $-P_3$  increase with an increasing shear rate. The particle property changes with accumulated energy are similar from shear rate to shear rate, with the largest shear rate generally producing the most significant effects.

#### 4. Discussion

The experiments in this study were designed to evaluate the effects of increasing shear rate on the structure of boehmite aggregate suspensions. The Peclet number (Eq. (4)) provides an estimate of the relative importance of hydrodynamic shear on the boehmite particles. This was calculated as a function of  $\dot{\gamma}_{\text{avg}}$  for the 200 nm aggregate (Table 1). The  $Pe$  values for a 9 nm particle (i.e., unified fit level 1) were less than or on the order of 1 for all cases. This indicates that Brownian forces will dominate over shear forces,

possibly inducing aggregation of 9 nm particles. However, the invariant behavior of the level 1 parameters during cycling suggests negligible aggregation for 9 nm particles.

#### 4.1. Initial conditions

The first run (A) had the lowest Peclet number (1.9, Table 1) of the experiments conducted. Thus, the influence of flow is expected to be lowest for run A. Indeed, values for  $\eta_{sus}$ , particle size ( $R_{g,i}$ ), and the fractal dimension ( $-P_i$ ) were nearly constant, allowing for run A to serve as an initial reference state for the boehmite particle suspensions. This can then be compared with both experiments at higher shear rates and previous experiments by Nakouzi [43] et al. and Anovitz [42] et al. that studied the aggregation of boehmite nanoparticles (ranging from 0.01 to 20 wt%) under similar chemical conditions without flow.

The multi-level unified fit model assumes that level 1 particles cluster to form larger boehmite aggregates represented by level 2. For run A the initial size of the level 2 aggregates ( $R_{g,2}^0$ ) was  $2510 \pm 250 \text{ \AA}$  (Table 2). This remained nearly constant for about 20 cycles (5 h), after which it increased to approximately  $3200 \text{ \AA}$  (Fig. 4). The initial mass fractal dimension  $d_f$  ( $-P_i$ ) was  $2.07 \pm 0.01$  (Table 2). This decreased slowly during the experiment to  $2.04 \pm 0.01$  (Fig. 5), which is larger than the value predicted for aggregates composed of spherical building blocks (1.5–1.9) [19], and smaller than those given by Anovitz et al. for equilibrated salt-free samples with 20 wt% solid ( $2.537 \pm 0.016$ ) [42], and Nakouzi et al. ( $2.3 \pm 0.18$ ) [43] for 0.01 wt% boehmite at pH 12 and  $\text{NaNO}_3$  concentrations from 0.01 to 0.1 mol  $\text{dm}^{-3}$ . The deviation of  $d_f$  from that predicted for aggregates composed of spherical building blocks suggests that orientationally-dependent interactions may be important. However, the largest agglomerates (level 3) had an initial  $d_f$  of  $1.6 \pm 0.4$  (Fig. 6), similar to values expected for spherical particles, implying that the orientational dependence of the hydrodynamic and van der Waals forces decreases as the aggregate size increases, perhaps implying limited asymmetry in the initial level 2 aggregates. This parameter increased over the first seven cycles (2 h), then became approximately constant at a value of  $2.2 \pm 0.4$ . This is slightly smaller than, but within uncertainty of, the value reported by Anovitz et al. [42] ( $2.37 \pm 0.11$ ). This implies growing three-dimensional complexity of the level 3 agglomerates as the slurry is cycled at this  $Pe$  value.

#### 4.2. Shear thinning

The viscosity of the suspension,  $\eta_{sus}$ , is, in principle, dependent on several physicochemical parameters including the particle volume fraction ( $\phi$ ), surface potentials, ionic strength, and the Hamaker constant ( $A_H$ ). For a 2.5 wt% boehmite suspension, the number density of the solid particles ( $2.4 \times 10^{17} \text{ m}^{-3}$ ) yields a value for  $\phi$  of  $\approx 0.008$ . Models for hard-sphere suspensions with a low volume fraction (e.g. studies by Einstein and Batchelor) [20,23] predict that  $\eta_{sus}$  should be very close to the solvent viscosity (i.e. 1 mPa s). Batchelor [23] showed that the ratio of suspension viscosity to solvent viscosity at  $\phi \ll 1$  is  $1 + 2.5\phi + 6.2\phi^2$  for a hard-sphere suspension, which yields a value of 1.02 for the boehmite suspension (orange dashed line in Fig. 7). Furthermore, appreciable shear-thinning is also unexpected [61] because there are few inter-particle interactions.

However, this is not what was observed in these experiments. The boehmite suspensions investigated undergo noticeable shear-thinning, as evidenced by the decrease in  $\eta_{sus,i}$  as a function of increasing  $Pe$  (Table 1, blue circles in Fig. 7). This indicates a significant deviation from hard-sphere behavior, consistent with the results of Nakouzi et al. [43], who demonstrated that boehmite

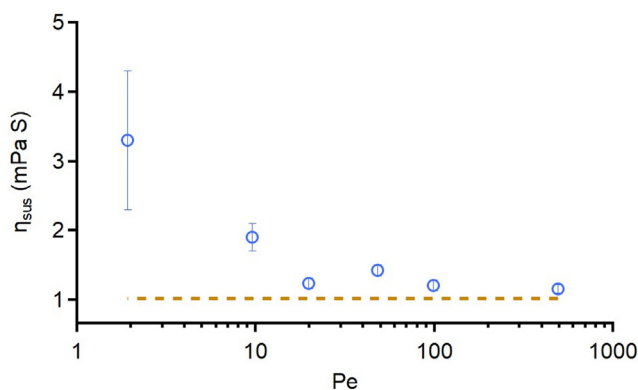


Fig. 7. The experimental  $\eta_{sus}$  values (blue circles, average  $\pm 2\sigma$ ) as a function of  $Pe$ . The dashed line denotes the prediction from the hard sphere-based model at a low volume fraction by Batchelor [23].

particles experience strong interactions even at low volume fractions in the absence of flow. This, in fact, is analogous to the observation of extremely large  $\eta_{sus}$  at low  $Pe$  for spherical particle suspensions with strong electrostatic repulsions at low ionic strength [21], in which a large inverse Debye length allows particles to interact at large separations. In this case, the electrostatic repulsive force is likely insignificant, as the PZC of boehmite is very close to the pH of the experiment (pH = 9) [44,45]. Therefore, the increase in  $\eta_{sus}$  ( $3.3 \pm 0.5 \text{ mPa s}$ , Table 1) at low  $Pe$  with a small solid volume fraction can likely be attributed to orientation-dependent interactions arising from the non-spherical, plate-like shape of the boehmite particles (Fig. S1). This will only remain the case, however, as long as no external force disturbs the inter-particle orientations. Thus, as the shear force increases (i.e. increasing  $Pe$ ), the effect of particle interactions decreases and the suspension viscosity can be expected to approach that of hard-sphere suspensions, which it does (Fig. 7). Interestingly, however, the influence of particle interactions on viscosity is still noticeable at  $Pe \approx 10$ , implying that significant shear energy is needed to overcome the asymmetric particle–particle interactions.

#### 4.3. Pre-shear effects on aggregate properties

The effect of the pre-shearing cycle on the level 2 aggregates can be observed by comparing the initial particle sizes (Table 2). Excluding run E, the  $R_{g,2}^0$  values decreased from  $2510 \pm 250 \text{ \AA}$  to  $1320 \pm 80 \text{ \AA}$  as a function of  $Pe$  (Fig. 8(A)), indicative of aggregate fragmentation. Fragmentation can only occur if the hydrodynamic force is larger than the binding force holding the particles together (i.e., a critical shear rate ( $\dot{\gamma}_{cr}$ ) must be exceeded). The incremental fragmentation shown in Fig. 8(A) suggests that multiple  $\dot{\gamma}_{cr}$  exist that correspond to binding forces of varying strengths. As the hydrodynamic force is increased, more binding forces are overcome, producing more fragmentation. This is in contrast to what might be expected if a single binding force held the aggregates together, where fragmentation would occur at a single point, when  $\dot{\gamma} > \dot{\gamma}_{cr}$ . Therefore, after preparation, weakly bound aggregates exist in the suspension with a distribution of binding forces. This distribution of forces may correspond to the different configurations that the non-spherical aggregate subunits can adopt, which would have binding strengths dependent on the arrangement and orientation of the subunits.

The pre-shearing cycle also affected the initial shape of the level 3 agglomerates (red squares, Fig. 8(B)). An increase in  $d_f$  from 1.5 to 3.3 was observed with increasing hydrodynamic shear force, indicating restructuring of the level 3 agglomerates into denser shapes. The incremental influence of flow rate on particle shape

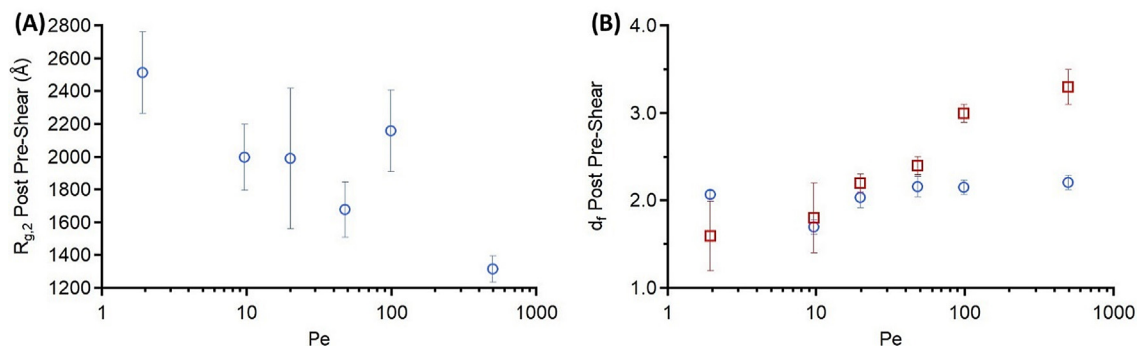


**Fig. 8.** (A) The initial size of the level 2 aggregates decreases with an increasing influence of the hydrodynamic force (represented by  $Pe$ ). (B) The fractal dimensions for level 2 (blue circles) and level 3 (red squares) aggregates are shown after the pre-shearing cycle for each run. The errors for both (A) and (B) are the same as those given in Table 2. (For interpretation of the references to colour in this figure legend, the reader is referred to the web version of this article.)

is analogous to the influence of shear force on aggregate size discussed previously. Since the size and shape of the aggregates are likely to be correlated for non-spherical particles, and the system is polydisperse in both size and shape, it is expected that the shear force will have an incremental effect on the shape of the aggregates as the distribution of critical shear rates are overcome. However, the relatively abrupt change in  $d_{f,3}$  between runs D and E suggests that this polydispersity may not completely smear out the effects of the critical shear rate on the aggregate structure. The change in  $d_{f,3}$  also suggests that  $R_{g,3}^0$  will also decrease with increasing hydrodynamic shear force. However, as noted above, the limited scale range of the USAXS prevents us from definitively determining if there was a change in  $R_{g,3}^0$ , although the data do suggest that it decreases. By comparison, the initial shape of the level 2 aggregates did not change with increasing hydrodynamic shear force (blue circles, Fig. 8(B)). Therefore, while the hydrodynamic shearing at larger shear rates was strong enough to break apart the level 3 agglomerates, the level 2 aggregates retained their shape after the initial pre-shearing cycle.

The size of the level 2 aggregates can also be correlated with the energy dissipation (Table S1) determined from the CFD simulations (Fig. 9). This permits an estimate of the aggregate bonding strength to be obtained by assuming that each incremental increase in energy dissipation per half cycle is able to overcome stronger attractive forces. Therefore, Fig. 9 may be an example of the distribution of level 2 aggregate attractive forces. The plot should level out as the energy dissipation decreases and hydrodynamic forces become too weak to overcome the interparticle attractive forces. Conversely, as the energy increases the size of the level 2 aggregates should eventually approach that of the level

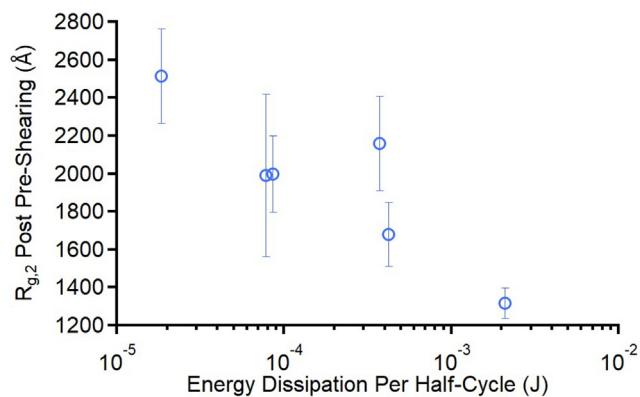


**Fig. 9.** The size of the level 2 aggregates decreases with higher energy half-cycles.

1 aggregates as the level 2 aggregates are destroyed. However, neither of these terminal behaviors were observed.

#### 4.4. Slurry cycling effects

The results from run A, where  $Pe \approx 2$  indicate that, under a minimal influence of flow, boehmite particles form aggregates of multiple sizes. Depending on the circumstances, however, flow can promote either aggregation or fragmentation [1,62]. Flow can promote aggregation by increasing the aggregation rate ( $k_{agg}$ ) of an unstable dispersion or mechanically destabilizing a dispersion resistant to Brownian aggregation [20]. Conversely, if the hydrodynamic shear forces are larger than the van der Waals attractive force, flow can cause fragmentation [36].

Significant changes were observed in the level 2 aggregates for each run. The  $Pe$  of the 200 nm aggregates ranged from  $\approx 2 - 480$ , depending on  $\dot{\gamma}_{avg}$ . For runs A - C the Peclet number was less than 20 (Table 1), indicating that the influence of hydrodynamic forces was moderate compared to Brownian forces. These experiments monitored sizes between  $\approx 6$  and 2000 Å using USAXS, SAXS, and WAXS. For these three runs the scattering data showed no significant changes at any length scale during cycling, indicating that the suspensions reached an apparent steady state during flow. Indeed, the  $R_{g,2}$ ,  $P_2$ , and  $P_3$  for runs A - C were nearly invariant during the cycling of the slurry (Figs. 4–6), although some changes are observed (particularly  $P_3$  for run C). Thus, the weakly bound aggregates discussed above probably still exist in these runs after pre-shearing. The constant value of  $\eta_{sus}$  during cycling supports this view. While  $\eta_{sus}$  may have increased slightly in run C (Fig. 2), the trend is unclear and may reflect the equally scattered increasing trend in  $R_{g,2}$  shown in Fig. 4 (run C,  $600 \text{ s}^{-1}$ ).

While the changes in the structures of the lower  $Pe$  experiments were generally small, the higher  $Pe$  experiments such as runs D and F showed significant variations in the size and shape of the level 2 aggregates during flow. The  $Pe$  values for the 200 nm aggregates were 47 and 480 for runs D and F, respectively, implying an increase in the importance of hydrodynamic forces relative to Brownian forces on aggregation relative to runs A-C ( $Pe$  ranging from 1.9 - 19). In runs D and F  $R_{g,2}$  increased and the fractal dimension,  $-P_2$ , decreased with increasing numbers of cycles (accumulated energy, Figs. 4 and 5). In run E, however, there was no obvious change in  $R_{g,2}$ , although  $-P_2$  again decreased. In order to explain these changes in level 2 aggregation, it is important to consider the fragmentation of the 3rd level, composed of larger agglomerates with a radius of gyration beyond the range of the USAXS instrument. The  $\dot{\gamma}_{cr}$  decreases with increasing particle size [20]. Based on a spherical approximation, this can be estimated from a balance between the van der Waals force:

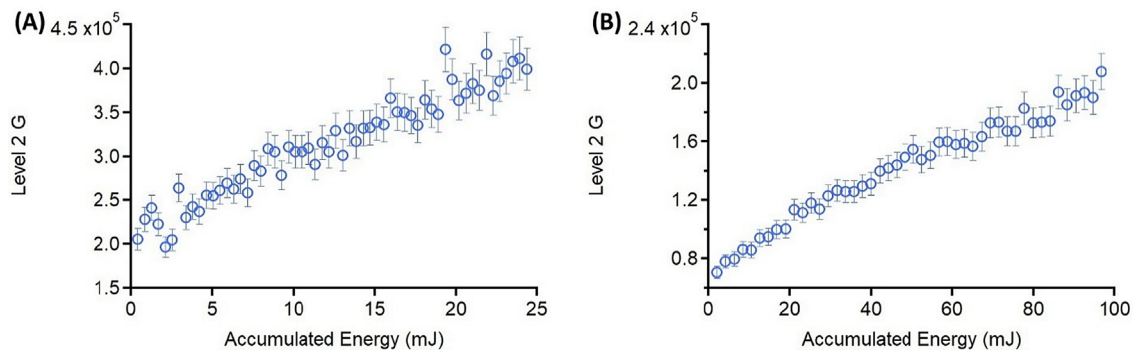


**Fig. 10.** The unified fit parameter  $G$  is proportional to the number of level 2 aggregates. The number of level 2 aggregates increases during the slurry cycling for runs **D** (A) and **F** (B).

$$F_{vdW} = -\frac{A_H a}{12h^2} \quad (10a)$$

and the hydrodynamic shear force,

$$F_{shear} = 6\pi\mu a^2\dot{\gamma} \quad (10b)$$

where  $h$  is a characteristic separation between particles within the aggregate,  $A_H$  is the Hamaker constant,  $a$  is the apparent size of the particle, and  $\mu$  is the solvent viscosity. Assuming that  $h \approx 0.1a$ ,  $\dot{\gamma}_{cr} \approx A_H/(\pi\mu a^3)$ , and  $A_H = 5.2kT$  [43], the fragmentation of the agglomerates (level 3) is likely to occur at values of  $\dot{\gamma} > 1400 \text{ s}^{-1}$ , the value estimated for experiment **D** (Table 1). Under these conditions hydrodynamic forces can overcome the attractive van der Waals forces. While not fully quantitative, the USAXS results (Fig. S8) indicate that fragmentation of the agglomerates did occur during cycling. The  $R_{g,3}$  shifts to smaller values just at the edge of the USAXS instrument's measurable  $Q$  range as the shearing force is increased. Although there is not enough of the region visible for an accurate fit to be obtained using the unified fit model, this shift is a good indicator that the  $F_{shear}$  is incrementally overcoming  $F_{vdW}$  at the agglomerate scale.

This is also observed indirectly from the increase in the size (Fig. 4) and relative intensity ( $G_2$ , Eq. (6)) of level 2 aggregates for runs **D** and **F** (Fig. 10), which is correlated to the number of scattering objects of a given size range (level) [52,59]. As the value of  $G_2$  increased with accumulated energy for experiments **D** and **F**, the number of level 2 aggregates also increased, likely from fragmentation of large (level 3) agglomerates.

As the results suggest that fragmentation of larger agglomerates ( $>3000 \text{ \AA}$ ) increased the number and size of the level 2 aggregates ( $\approx 2000 \text{ \AA}$ ) in runs **D** and **F**, the hydrodynamic force must have been sufficient to induce fragmentation of the agglomerates, but not strong enough in the shear rate range investigated to break up the aggregates at the level 2 scale (note that  $\dot{\gamma}_{cr}$  scales as  $1/a^3$  with an estimated  $\dot{\gamma}_{cr} \approx 609 \text{ s}^{-1}$  for a  $2500 \text{ \AA}$  particle). In addition, at level 2 length scales ( $\approx 2000 \text{ \AA}$ ), aggregation was induced by the imposed shear, along with a minor effect from Brownian forces. However, the time scale of the shear ( $\dot{\gamma}_{avg}^{-1}$ ) is approximately ten times that of motions induced by Brownian forces ( $D_r^{-1}$ ), where  $D_r$  denotes the rotational diffusivity of the particle (see SI). This implies that, under shear, the particles do not have enough time to find energetically favorable configurations, leading to the irregular aggregate shapes being adopted by the boehmite particle aggregates [43]. This phenomenon may be reflected in the decrease in the level 2 mass fractal dimensions ( $-P_2$ ) for runs **D** and **F** (Fig. 5). As mentioned previously, the initial  $-P_2$  values of  $2.16 \pm 0.03$  and  $2.18 \pm 0.02$  (Table 2) were larger than expected for colloids composed of spherical particles (1.5–1.9) [19], indicative of shape anisotropy of the primary

particles that cluster to form the level 2 aggregates. The decrease in the fractal dimension during cycling may suggest characteristics of shear-induced aggregation (e.g., alignment of boehmite particles having stacked configurations with the shear flow). However, the aggregates appear to retain their shape anisotropy, even at the end of the cycling, as final fractal dimensions do not reach those of spherical colloids. The retention of these shape irregularities and residual orientation-dependent forces may explain the mild increase in suspension viscosity during cycling for runs **D** and **F** (Fig. 2). The fragmentation of level 3 agglomerates into irregularly shaped level 2 aggregates should increase the influence of orientation-dependent interactions in the slurry, increasing the number of particles with large “apparent” repulsions, increasing  $\eta_{sus}$  at low  $\phi$  and ionic strength.

## 5. Summary and Conclusions

Using a combination of USAXS, SAXS, WAXS and *in-situ* capillary rheometry at different flow conditions, the rheological responses of relatively dilute boehmite suspensions (2.5 wt% solid and pH 9) and their correlations with aggregation/fragmentation under flow were studied. A relatively wide range of flow conditions, characterized by Peclet numbers ranging from 1.9 to 480, enabled determination of both boehmite aggregation and rheological response under conditions ranging from little to significant flow control of aggregate structure. Shear-thinning was clearly observed and explained by orientation-dependent interactions that arise from the non-spherical boehmite particles that compose the aggregates. This demonstrates that orientation-dependent interactions can lead to measurable rheological responses, analogous to the aforementioned effect of decreasing electrolyte concentrations.

While aggregation under flow has been studied for a number of cases [63,64], fragmentation under flow is much less well understood due to the complexities of the process. At large  $Pe$  a modest increase in suspension viscosity was observed over the course of a few hours of cycling. This was correlated with a complicated interplay between aggregate scales via aggregation/fragmentation (i.e. increasing sizes and relative amounts of level 2 aggregates and fragmentation of level 3 agglomerates). The restructuring of level 3 agglomerates resulted in an increase in the size and complexity of the non-spherical level 2 aggregates, which may contribute to the orientation-dependent interactions, thus explaining the increase in suspension viscosity.

Future work will explore this phenomenon at larger mass fractions, where the effect is expected to be more complex, as well as under different chemical conditions (e.g. increased pH, cation and anion size, charge, and concentration). In addition, determining the energy dissipation per cycle obtained using CFD also provided

a means to estimate the strength of aggregate attractive forces. As suggested by Anovitz et al. [42], more complex rheological properties, such as coupling between orientational-dependent particle interactions and hindering of particle motions from nearby particles would be expected at higher solid concentrations (20 wt%). Understanding the coupling between ionic interactions (e.g. larger ionic strengths or pH) and orientation-dependent interactions under flow will enhance our ability to control and predict rheology in many industrial applications, including transfer and treatment of Hanford wastes.

### CRedit authorship contribution statement

**Anthony J. Krzysko:** Methodology, Formal analysis, Investigation, Writing - original draft, Writing - review & editing. **Elias Nakouzi:** Formal analysis, Writing - review & editing. **Xin Zhang:** Resources. **Trent R. Graham:** Resources. **Kevin M. Rosso:** Writing - review & editing. **Gregory K. Schenter:** Formal analysis, Writing - review & editing. **Jan Ilavsky:** Methodology, Formal analysis. **Ivan Kuzmenko:** Methodology, Resources. **Matthew G. Frith:** Methodology, Resources. **Cornelius F. Ivory:** Writing - original draft, Writing - review & editing, Formal analysis. **Sue B. Clark:** Writing - original draft, Funding acquisition. **Javen S. Weston:** Methodology, Formal analysis. **Katie M. Weigandt:** Supervision, Data curation. **James J. De Yoreo:** Conceptualization, Formal analysis. **Jaehun Chun:** Conceptualization, Writing - original draft, Formal analysis, Writing - review & editing, Project administration. **Lawrence M. Anovitz:** Conceptualization, Formal analysis, Writing - original draft, Writing - review & editing, Investigation, Methodology, Project administration.

### Declaration of Competing Interest

The authors declare that they have no known competing financial interests or personal relationships that could have appeared to influence the work reported in this paper.

### Acknowledgements

This research was supported by the Interfacial Dynamics in Radioactive Environments and Materials (IDREAM), an Energy Frontier Research Center funded by the U.S. Department of Energy, Office of Science, Basic Energy Sciences. PNNL is a multiprogram national laboratory operated for DOE by Battelle Memorial Institute under Contract No. DE-AC05-76RL0-1830. This research used resources of the Advanced Photon Source, a U.S. Department of Energy (DOE) Office of Science User Facility operated for the DOE Office of Science by Argonne National Laboratory under Contract No. DE-AC02-06CH11357. A.J.K. is grateful for the support from the PNNL-WSU DGRP and the DOE-SCGSR. This material is based upon work supported by the U.S. Department of Energy, Office of Science Graduate Student Research (SCGSR) program. The SCGSR program is administered by the Oak Ridge Institute for Science and Education (ORISE) for the DOE. ORISE is managed by ORAU under contract number DE-SC0014664. All opinions expressed in this paper are the author's and do not necessarily reflect the policies and views of DOE, ORAU, or ORISE. Mention of commercial products in this work is not intended to imply any endorsement or recommendation by the National Institute of Standards and Technology.

### Appendix A. Supplementary material

Supplementary data to this article can be found online at <https://doi.org/10.1016/j.jcis.2020.04.016>.

### References

- [1] P. Jarvis, B. Jefferson, J. Gregory, S.A. Parsons, A review of Floc strength and breakage, *Water Res.* 39 (14) (2005) 3121–3137, <https://doi.org/10.1016/j.watres.2005.05.022>.
- [2] Y. Kikuchi, H. Yamada, H. Kunimori, T. Tsukada, M. Hozawa, C. Yokoyama, M. Kubo, Aggregation behavior of latex particles in shear flow confined between two parallel plates, *Langmuir* 21 (8) (2005) 3273–3278, <https://doi.org/10.1021/la048011j>.
- [3] W.J. Batchelor, J. He, W.W. Sampson, Inter-fibre contacts in random fibrous materials: experimental verification of theoretical dependence on porosity and fibre width, *J. Mater. Sci.* 41 (24) (2006) 8377–8381, <https://doi.org/10.1007/s10853-006-0889-7>.
- [4] I.B. Bekard, P. Asimakis, J. Bertolini, D.E. Dunstan, The effects of shear flow on protein structure and function, *Biopolymers* 95 (11) (2011) 733–745, <https://doi.org/10.1002/bip.21646>.
- [5] R. van der Kant, A.R. Karow-Zwick, J. Van Durme, M. Blech, R. Gallardo, D. Seeliger, K. Alßfalg, P. Baatsen, G. Compennolle, A. Gils, J.M. Studts, P. Schulz, P. Garidel, J. Schymkowitz, F. Rousseau, Prediction and reduction of the aggregation of monoclonal antibodies, *J. Mol. Biol.* 429 (8) (2017) 1244–1261, <https://doi.org/10.1016/j.jmb.2017.03.014>.
- [6] R.C. Elgebrandt, J.A. Romagnoli, D.F. Fletcher, V.G. Gomes, R.G. Gilbert, Analysis of shear-induced coagulation in an emulsion polymerisation reactor using computational fluid dynamics, *Chem. Eng. Sci.* 60 (7) (2005) 2005–2015, <https://doi.org/10.1016/j.ces.2004.12.010>.
- [7] G. Frungieri, M. Vanni, Shear-induced aggregation of colloidal particles: a comparison between two different approaches to the modelling of colloidal interactions, *Can. J. Chem. Eng.* 95 (9) (2017) 1768–1780, <https://doi.org/10.1002/cjce.22843>.
- [8] S. Lazzari, L. Nicoud, B. Jaquet, M. Lattuada, M. Morbidelli, Fractal-like structures in colloid science, *Adv. Colloid Interface Sci.* 235 (2016) 1–13, <https://doi.org/10.1016/j.cis.2016.05.002>.
- [9] S. Caimi, A. Cingolani, B. Jaquet, M. Siggel, M. Lattuada, M. Morbidelli, Tracking of fluorescently labeled polymer particles reveals surface effects during shear-controlled aggregation, *Langmuir* 33 (49) (2017) 14038–14044, <https://doi.org/10.1021/acs.langmuir.7b03054>.
- [10] J. Dobson, A. Kumar, L.F. Willis, R. Tuma, D.R. Higazi, R. Turner, D.C. Lowe, A.E. Ashcroft, S.E. Radford, N. Kapur, D.J. Brockwell, Inducing protein aggregation by extensional flow, *Proc. Natl. Acad. Sci.* 114 (18) (2017) 4673–4678, <https://doi.org/10.1073/pnas.1702724114>.
- [11] M. Boström, V. Demiz, G.V. Franks, B.W. Ninham, Extended DLVO theory: electrostatic and non-electrostatic forces in oxide suspensions, *Adv. Colloid Interface Sci.* 123–126 (SPEC. ISS.) (2006) 5–15, <https://doi.org/10.1016/j.cis.2006.05.001>.
- [12] M. Boström, D.R.M. Williams, B.W. Ninham, Specific Ion Effects: Why DLVO Theory Fails for Biology and Colloid Systems 168103/1–168103/4, *Phys. Rev. Lett.* 87 (16) (2001), <https://doi.org/10.1103/PhysRevLett.87.168103>.
- [13] T. Cao, G. Trefalt, M. Borkovec, Aggregation of colloidal particles in the presence of hydrophobic anions: importance of attractive non-DLVO forces, *Langmuir* 34 (47) (2018) 14368–14377, <https://doi.org/10.1021/acs.langmuir.8b03191>.
- [14] R.M. Pashley, DLVO and hydration forces between mica surfaces in Li<sup>+</sup>, Na<sup>+</sup>, K<sup>+</sup>, and Cs<sup>+</sup> electrolyte solutions: a correlation of double-layer and hydration forces with surface cation exchange properties, *J. Colloid Interface Sci.* 83 (2) (1981) 531–546, [https://doi.org/10.1016/0021-9797\(81\)90348-9](https://doi.org/10.1016/0021-9797(81)90348-9).
- [15] T. Oncsik, G. Trefalt, M. Borkovec, I. Szilagy, Specific ion effects on particle aggregation induced by monovalent salts within the Hofmeister series, *Langmuir* 31 (13) (2015) 3799–3807, <https://doi.org/10.1021/acs.langmuir.5b00225>.
- [16] A.M. Smith, A.A. Lee, S. Perkin, The electrostatic screening length in concentrated electrolytes increases with concentration, *J. Phys. Chem. Lett.* 7 (12) (2016) 2157–2163, <https://doi.org/10.1021/acs.jpcllett.6b00867>.
- [17] M.A. Gebbie, A.M. Smith, H.A. Dobbs, A.A. Lee, G.G. Warr, X. Banquy, M. Valtiner, M.W. Rutland, J.N. Israelachvili, S. Perkin, R. Atkin, Long range electrostatic forces in ionic liquids, *Chem. Commun.* 53 (7) (2017) 1214–1224, <https://doi.org/10.1039/c6cc08820a>.
- [18] Z. He, P. Alexandridis, Nanoparticles in ionic liquids: interactions and organization, *Phys. Chem. Chem. Phys.* 17 (28) (2015) 18238–18261, <https://doi.org/10.1039/c5cp01620g>.
- [19] M.Y. Lin, H.M. Lindsay, D.A. Weitz, R.C. Ball, R. Klein, P. Meakin, Universality in colloid aggregation, *Nature* 339 (6223) (1989) 360–362, <https://doi.org/10.1038/339360a0>.
- [20] W.B. Russel, D.A. Saville, W.R. Schowalter, *Colloidal Dispersions* (1989), <https://doi.org/10.1017/CBO9780511608810>.
- [21] I.M. Krieger, M. Eguiluz, The second electroviscous effect in polymer latices, *Trans. Soc. Rheol.* 20 (1) (1976) 29–45, <https://doi.org/10.1122/1.549428>.
- [22] R. Buscall, J.W. Goodwin, M.W. Hawkins, R.H. Ottewill, Viscoelastic Properties of Concentrated Latices. Part 2.—Theoretical Analysis, *J. Chem. Soc. Faraday Trans. 1 Phys. Chem. Condens. Phases* 78 (1) (1982) 2889, <https://doi.org/10.1039/f19827802889>.
- [23] G.K. Batchelor, The effect of brownian motion on the bulk stress in a suspension of spherical particles, *J. Fluid Mech.* 83 (1) (1977) 97–117, <https://doi.org/10.1017/S0022112077001062>.
- [24] A. Zaccone, M. Soos, M. Lattuada, H. Wu, M.U. Bäbler, M. Morbidelli, Breakup of dense colloidal aggregates under hydrodynamic stresses, *Phys. Rev. E - Stat.*

- Nonlinear, *Soft Matter Phys.* 79 (6) (2009), <https://doi.org/10.1103/PhysRevE.79.061401>.
- [25] H. Hodne, A. Saasen, A.B. O'Hagan, S.O. Wick, Effects of time and shear energy on the rheological behaviour of oilwell cement slurries, *Cem. Concr. Res.* 30 (11) (2000) 1759–1766, [https://doi.org/10.1016/S0008-8846\(00\)00416-6](https://doi.org/10.1016/S0008-8846(00)00416-6).
- [26] R.B. Moruzzi, A.L. de Oliveira, F.T. da Conceição, J. Gregory, L.C. Campos, Fractal dimension of large aggregates under different flocculation conditions, *Sci. Total Environ.* 609 (2017) 807–814, <https://doi.org/10.1016/j.scitotenv.2017.07.194>.
- [27] D.K. Rai, G. Beaucage, E.O. Jonah, D.T. Britton, S. Sukumaran, S. Chopra, G.G. Gonfa, M. Härting, Quantitative investigations of aggregate systems, *J. Chem. Phys.* 137 (4) (2012) 574–588, <https://doi.org/10.1063/1.4737947>.
- [28] C.M. Sorensen, Light scattering by fractal aggregates: a review, *Aerosol Sci. Technol.* 35 (2) (2001) 648–687, <https://doi.org/10.1080/02786820117868>.
- [29] J. Mewis, N.J. Wagner, Thixotropy, *Adv. Colloid Interface Sci.* 147–148 (2009) 214–227, <https://doi.org/10.1016/j.cis.2008.09.005>.
- [30] F. Peyronel, B. Quinn, A.G. Marangoni, D.A. Pink, Ultra small angle X-ray scattering in complex mixtures of triacylglycerols, *J. Phys. Condens. Matter* 26 (46) (2014), <https://doi.org/10.1088/0953-8984/26/46/464110> 464110.
- [31] B.J. Maranzano, N.J. Wagner, Flow-small angle neutron scattering measurements of colloidal dispersion microstructure evolution through the shear thickening transition, *J. Chem. Phys.* 117 (22) (2002) 10291–10302, <https://doi.org/10.1063/1.1519253>.
- [32] D. Alaimo, D. Hermida Merino, B. Grignard, W. Bras, C. Jérôme, A. Debuigne, C.J. Gommès, Small-angle X-ray scattering insights into the architecture-dependent emulsifying properties of amphiphilic copolymers in supercritical carbon dioxide, *J. Phys. Chem. B* 119 (4) (2015) 1706–1716, <https://doi.org/10.1021/jp5086558>.
- [33] H. Katepalli, V.T. John, A. Tripathi, A. Bose, Microstructure and rheology of particle stabilized emulsions: effects of particle shape and inter-particle interactions, *J. Colloid Interface Sci.* 485 (2017) 11–17, <https://doi.org/10.1016/j.jcis.2016.09.015>.
- [34] M. Zeidan, B.H. Xu, X. Jia, R.A. Williams, Simulation of aggregate deformation and breakup in simple shear flow using a combined continuum and discrete model, *Chem. Eng. Res. Des.* 85 (12 A) (2007) 1645–1654, [https://doi.org/10.1016/S0263-8762\(07\)73208-2](https://doi.org/10.1016/S0263-8762(07)73208-2).
- [35] Y.M. Harshe, M. Lattuada, Breakage rate of colloidal aggregates in shear flow through stokesian dynamics, *Langmuir* 28 (1) (2012) 283–292, <https://doi.org/10.1021/la2038476>.
- [36] Y.M. Harshe, M. Lattuada, M. Soos, Experimental and modeling study of breakage and restructuring of open and dense colloidal aggregates, *Langmuir* 27 (10) (2011) 5739–5752, <https://doi.org/10.1021/la1046589>.
- [37] R.E. Gephart, A short history of waste management at the hanford site, *Phys. Chem. Earth* 35 (6–8) (2010) 298–306, <https://doi.org/10.1016/j.pce.2010.03.032>.
- [38] R.A. Peterson, G.J. Lumetta, B.M. Rapko, A.P. Poloski, Modeling of boehmite leaching from actual hanford high-level waste samples, *Sep. Sci. Technol.* 42 (8) (2007) 1719–1730, <https://doi.org/10.1080/01496390701242111>.
- [39] R.A. Peterson, E.C. Buck, J. Chun, R.C. Daniel, D.L. Herting, E.S. Ilton, G.J. Lumetta, S.B. Clark, Review of the scientific understanding of radioactive waste at the U.S. DOE hanford site, *Environ. Sci. Technol.* 52 (2) (2018) 381–396, <https://doi.org/10.1021/acs.est.7b04077>.
- [40] J. Bowers, C.P. Butts, P.J. Martin, M.C. Vergara-Gutierrez, R.K. Heenan, Aggregation behavior of aqueous solutions of ionic liquids, *Langmuir* 20 (6) (2004) 2191–2198, <https://doi.org/10.1021/la035940m>.
- [41] Y. Hatwalne, S. Ramaswamy, M. Rao, R.A. Simha, Rheology of active-particle suspensions, *Am. Phys. Soc.* 92 (11) (2003) 118101–118102, <https://doi.org/10.1103/PhysRevLett.92.118101>.
- [42] L.M. Anovitz, X. Zhang, J. Soltis, E. Nakouzi, A.J. Krzysko, J. Chun, G.K. Schenter, T.R. Graham, K.M. Rosso, J.J. De Yoreo, A.G. Stack, M. Bleuel, C. Gagnon, D.F.R. Mildner, J. Ilavsky, I. Kuzmenko, Effects of ionic strength, salt, and pH on aggregation of boehmite nanocrystals: tumbler small-angle neutron and X-ray scattering and imaging analysis, *Langmuir* 34 (51) (2018) 15839–15853, <https://doi.org/10.1021/acs.langmuir.8b00865>.
- [43] E. Nakouzi, J.A. Soltis, B.A. Legg, G.K. Schenter, X. Zhang, T.R. Graham, K.M. Rosso, L.M. Anovitz, J.J. De Yoreo, J. Chun, Impact of solution chemistry and particle anisotropy on the collective dynamics of oriented aggregation, *ACS Nano* 12 (10) (2018) 10114–10122, <https://doi.org/10.1021/acs.nano.8b04909>.
- [44] G.A. Parks, The isoelectric points of solid oxides, solid hydroxides, and aqueous hydroxo complex systems, *Chem. Rev.* 65 (2) (1965) 177–198, <https://doi.org/10.1021/cr60234a002>.
- [45] J. Chun, T. Oh, M. Luna, M. Schweiger, Effect of particle size distribution on slurry rheology: nuclear waste simulant slurries, *Colloids Surfaces A Physicochem. Eng. Asp.* 384 (1–3) (2011) 304–310, <https://doi.org/10.1016/j.colsurfa.2011.04.003>.
- [46] X. Zhang, W. Cui, K.L. Page, C.I. Pearce, M.E. Bowden, T.R. Graham, Z. Shen, P. Li, Z. Wang, S. Kerisit, A.T. N'Diaye, S.B. Clark, K.M. Rosso, Size and morphology controlled synthesis of boehmite nanoplates and crystal growth mechanisms, *Cryst. Growth Des.* 18 (6) (2018) 3596–3606, <https://doi.org/10.1021/acs.cgd.8b00394>.
- [47] J.S. Weston, J. Chun, G. Schenter, K. Weigandt, M. Zong, X. Zhang, K.M. Rosso, L. M. Anovitz, Connecting particle interactions to agglomerate morphology and rheology of boehmite nanocrystal suspensions, *J. Colloid Interface Sci.* 2020 (572) (2020) 328–339, <https://doi.org/10.1016/j.jcis.2020.03.109>.
- [48] J. Ilavsky, F. Zhang, R.N. Andrews, I. Kuzmenko, P.R. Jemian, L.E. Levine, A.J. Allen, Development of combined microstructure and structure characterization facility for in situ and operando studies at the advanced photon source, *J. Appl. Crystallogr.* 51 (2018) 867–882, <https://doi.org/10.1107/S160057671800643X>.
- [49] T. Li, A.J. Senesi, B. Lee, Small angle X-ray scattering for nanoparticle research, *Chem. Rev.* 116 (18) (2016) 11128–11180, <https://doi.org/10.1021/acs.chemrev.5b00690>.
- [50] J. Ilavsky, Nika: software for two-dimensional data reduction, *J. Appl. Crystallogr.* 45 (2) (2012) 324–328, <https://doi.org/10.1107/S0021889812004037>.
- [51] J. Ilavsky, P.R. Jemian, Irena: tool suite for modeling and analysis of small-angle scattering, *J. Appl. Crystallogr.* 42 (2) (2009) 347–353, <https://doi.org/10.1107/S0021889809002222>.
- [52] G. Beaucage, Approximations leading to a unified exponential/power-law approach to small-angle scattering, *J. Appl. Crystallogr.* 28 (6) (1995) 717–728, <https://doi.org/10.1107/S0021889895005292>.
- [53] B. Hammouda, Analysis of the Beaucage model, *J. Appl. Crystallogr.* 43 (6) (2010) 1474–1478, <https://doi.org/10.1107/S0021889810033856>.
- [54] B. Hammouda, A new guinier-porod model, *J. Appl. Crystallogr.* 43 (4) (2010) 716–719, <https://doi.org/10.1107/S0021889810015773>.
- [55] R.M. Fearn, T. Mullin, A.K. Cliffe, Nonlinear flow phenomena in a symmetric sudden expansion, *J. Fluid Mech.* 211 (1990) 595–608, <https://doi.org/10.1017/S0022112090001707>.
- [56] E. Sanmiguel-Rojas, T. Mullin, Finite-amplitude solutions in the flow through a sudden expansion in a circular pipe, *J. Fluid Mech.* 691 (2012) 201–213, <https://doi.org/10.1017/jfm.2011.469>.
- [57] R.B. Bird, B. Robert, W.E. Stewart, E.N. Lightfoot, *Transport Phenomena*, J. Wiley, 2007.
- [58] F. Zhang, J. Ilavsky, G.G. Long, J.P.G. Quintana, A.J. Allen, P.R. Jemian, Glassy carbon as an absolute intensity calibration standard for small-angle scattering, *Metall. Mater. Trans. A Phys. Metall. Mater. Sci.* 41 (5) (2010) 1151–1158, <https://doi.org/10.1007/s11661-009-9950-x>.
- [59] G. Beaucage, Small-angle scattering from polymeric mass fractals of arbitrary mass-fractal dimension, *J. Appl. Crystallogr.* 29 (2) (1996) 134–146, <https://doi.org/10.1107/S0021889895011605>.
- [60] P.R. Bevington, D.K. Robinson, *Data Reduction and Error Analysis*, 3rd ed., McGraw-Hill, New York, 2003.
- [61] J.J. Stickel, R.L. Powell, Fluid mechanics and rheology of dense suspensions, *Annu. Rev. Fluid Mech.* 37 (1) (2005) 129–149, <https://doi.org/10.1146/annurev.fluid.36.050802.122132>.
- [62] J. Chun, D.L. Koch, S.L. Rani, A. Ahluwalia, L.R. Collins, Clustering of aerosol particles in isotropic turbulence, *J. Fluid Mech.* 536 (2005) 219–251, <https://doi.org/10.1017/S0022112005004568>.
- [63] A.A. Filkova, A.A. Martyanov, A.K. Garzon Dasgupta, M.A. Panteleev, A.N. Sveshnikova, Quantitative dynamics of reversible platelet aggregation: mathematical modelling and experiments, *Sci. Rep.* 9 (1) (2019) 6217, <https://doi.org/10.1038/s41598-019-42701-0>.
- [64] D.L. Marchisio, M. Soos, J. Sefcik, M. Morbidelli, Role of turbulent shear rate distribution in aggregation and breakage processes, *AIChE J.* 52 (1) (2006) 158–173, <https://doi.org/10.1002/aic.10614>.